Downloaded from ascelibrary.org by University of South Carolina on 08/20/25. Copyright ASCE. For personal use only; all rights reserved.

Fragility Curves for Highway Embankment Slope Stability under Extreme Rainfall

Ege Can Kurter, S.M.ASCE[1]; Mohammad Sadik Khan, M.ASCE[2]; Laura Micheli, A.M.ASCE[3]; Austin R.J. Downey, M.ASCE[4]; and Jasim Imran, F.ASCE[5]

Abstract: Highway embankment slopes are subject to potential failure due to extreme rainfall patterns. This study uses a fragility framework to examine the failure probability of a highway slope consisting of Yazoo clay in the northern part of Jackson, Mississippi, USA. A finite-element model of the slope is calibrated with available site data. Total rainfall depths between 47 mm and 630 mm are considered in the application of the model under different high-to-low intensity and short-to-long duration categories for return periods up to 1,000 years. Uncertainties in the rainfall patterns are incorporated through Monte Carlo simulation. The effects of extreme rainfall are integrated by applying the intensity and frequency of rainfall events that are greater than those of typical design considerations. Fragility curves, the continuous failure probability functions corresponding to a wide range of rainfall depths, are constructed using simulation outputs for different limit states. Rainfall duration is identified as the key factor affecting the embankment's fragility. Low-intensity and long-duration rainfalls are found to be more detrimental to the slope compared to high-intensity and short-duration rainfalls. This study revealed that the major limit state is only exceeded by post-200-mm rainfall depths, with an increasing exceedance likelihood at greater rainfall depths. Limit states showed higher exceedance probability from higher frequency rainfalls due to the long rebound period of Yazoo clay. The findings from this study may be utilized in the design of new embankments within the same region and in safety assessments of existing embankment slopes under a range of rainfall conditions. **DOI: 10.1061/NHREFO.NHENG-2248.** *© 2025 American Society of Civil Engineers.*

Practical Applications: The fragility curves developed through this study offer important insights for earthen infrastructure planning and design, enabling engineers to evaluate slope stability. Integrated with meteorological data, these curves can be instrumental in early warning systems when a projected rainfall event may threaten slope stability. Their applicability extends to maintenance schedules of vulnerable slopes, especially if a relatively high probability of failure is forecasted for future events.

Author keywords: Fragility curves; Slope stability; Highway embankments; Monte Carlo simulation; Extreme rainfall.

Introduction

Yazoo clay is a highly plastic soil commonly found in central Mississippi, USA. Many highway embankment fills are composed of this clay. The slopes of highway embankments constructed using highly plastic clay exhibit a softening behavior at the top surface over time, primarily attributed to the shrink-swell behavior from wet-dry cycles. During periods of heavy rainfall, these slopes are susceptible to failure due to the reduction in matric suction and soil strength. In the Jackson area, Yazoo clay exhibits an upper weathered zone above the unweathered clay (Taylor 2005). Due to its very low hydraulic conductivity, the top layer becomes fully saturated after prolonged wet periods (Khan et al. 2022). Engineering safety measures are applied to prevent slope failures during lengthy wet periods, such as applying H-piles and reconfiguring slopes to milder angles (Khan et al. 2022). Instances of shallow slope failures at highway embankment slopes, especially for Yazoo clay, are well-documented in the literature (e.g., Khan et al. 2017, 2019, 2022; Nobahar et al. 2019, 2020). Rainfall volume is a significant factor causing slope failure, leading to substantial maintenance budgets for repairs. Failure typically occurs either during or immediately after the rainfall (Tohari et al. 2007).

Fragility curves are graphical representations of the probability of a particular structural system reaching or exceeding a specific limit state due to varying levels of a hazard intensity measure. These curves have become critical in risk assessments, garnering significant attention primarily in seismic risk assessment. Contrary to traditional deterministic methods, which provide binary safety outcomes, fragility curves provide continuous probabilities across different hazard levels, offering a holistic risk assessment perspective. Fragility curves are widely used in risk assessment of civil structures subjected to seismic (e.g., Choi et al. 2004; Pan et al. 2007; Celik and Ellingwood 2008) and wind hazards (e.g., Rosowsky and Ellingwood 2002; Ellingwood et al. 2004; van de Lindt and Dao 2009; Micheli et al. 2019, 2020; Wang et al. 2022).

The use of fragility curves is now expanding to water resources and geotechnical engineering. For instance, Hall et al. (2003)

---

[1] Graduate Student, Dept. of Civil and Environmental Engineering, Univ. of South Carolina, 300 Main St., Columbia, SC 29208. ORCID: https://orcid.org/0000-0003-0273-0392. Email: kurter@sc.edu

[2] Associate Professor, Dept. of Civil and Environmental Engineering and Industrial Systems and Technology, Jackson State Univ., 1400 John R. Lynch St., Jackson, MS 39217. Email: sadik.khan@jsums.edu

[3] Research Assistant Professor, Dept. of Civil and Environmental Engineering, Univ. of South Carolina, 300 Main St., Columbia, SC 29208. ORCID: https://orcid.org/0000-0002-6806-3222. Email: lmicheli@mailbox.sc.edu

[4] Associate Professor, Dept. of Mechanical Engineering, Univ. of South Carolina, 300 Main St., Columbia, SC 29208. ORCID: https://orcid.org/0000-0002-5524-2416. Email: austindowney@sc.edu

[5] Professor, Dept. of Civil and Environmental Engineering, Univ. of South Carolina, 300 Main St., Columbia, SC 29208 (corresponding author). ORCID: https://orcid.org/0000-0002-3479-3905. Email: imran@sc.edu

Note. This manuscript was submitted on April 26, 2024; approved on May 13, 2025; published online on August 20, 2025. Discussion period open until January 20, 2026; separate discussions must be submitted for individual papers. This paper is part of the ***Natural Hazards Review***, © ASCE, ISSN 1527-6988.

Nat. Hazards Rev., 2025, 26(4): 04025052

constructed fragility curves for the national-scale flood risk assessments in the United Kingdom. These authors considered the overtopping and breaching failure modes of the earth structures. Apel et al. (2006) developed analytical fragility curves for levee breaching, in which the overtopping height and overflowing time are considered as load intensities. The developed fragility curve was used for the flood risk assessment of a section of the Rhine River. Vorogushyn et al. (2009) built analytical fragility curves for levees subjected to several failure modes. The authors accounted for the uncertainty of parameters influencing the breaching with a Monte Carlo simulation framework. Wu (2015) presented analytical and empirical fragility curves for slope stability based on first-order reliability and copula-based sampling methods. Wu's findings revealed the increased probability of failure resulting from greater inclination of the slope, higher rainfall infiltration, and higher earthquake intensity.

Jasim et al. (2017) investigated the effect of extreme precipitations on earthen levees by applying fully coupled stress-flow analysis to a finite-element model of the selected levee section. D'Oria et al. (2019) developed fragility curves for levees considering piping-induced breaching. Then, they used the fragility curves for the Po River flood hazard assessment. McKenna et al. (2021) constructed fragility curves for moisture ingress and scouring of highway embankments, considering the slope deformation as the measure of damage and water intensity as the load. The research confirmed the effect of higher groundwater levels on the increased vertical displacement of the embankment.

These studies constitute significant efforts to evaluate the hazard risk of levees and highway embankments. However, the fragility curves available in the literature are rarely informed by field data and do not consider the substantial state of the structure, which might have changed relative to the design conditions. This study proposes a framework to develop fragility curves of highway embankments based on a finite-element model calibrated with field data. This approach bridges the gap between theoretical models and actual conditions, offering a more precise tool for risk evaluation.

The proposed framework investigates the impact of rainfall conditions and matric suction distribution on slope failures. The following rainfall categories are defined to characterize the external hazard: high-intensity and short-duration, medium-intensity and medium-duration, and low-intensity and long-duration rainfalls. The magnitudes of the rainfalls are extracted from the National Oceanic and Atmospheric Administration's intensity-duration-frequency curves (NOAA 2013), considering return periods ranging from 50 years to 1,000 years for the Jackson area.

The contributions of this work are threefold: (1) incorporating actual site conditions into a fragility framework; (2) expanding the conventional use of fragility curves to highway embankments; and (3) examining the effects of extreme rainfall events on a representative slope.

Selected Study Area

The study site is located in the northern part of Jackson, Mississippi, at the intersection of US 80 and US I220 N highways. This site is selected due to the available data and geometry. The site location is depicted in Fig. 1. It is a 10-m-high slope, characterized by an angle of 4H:1V. Nobahar et al. (2019) determined a soil unit weight of 21 $\mathrm{kN/M^3}$ on this site. The unweathered clay layer begins at a depth of 6 m. The weathered top layer exhibits two different shear strength parameters. Therefore, it is divided into two layers: the top at residual strength and the middle at full softening. The magnitudes of the shear strength are based on the laboratory experiments of Khan et al. (2019). The shear strength magnitudes of the soil layers are

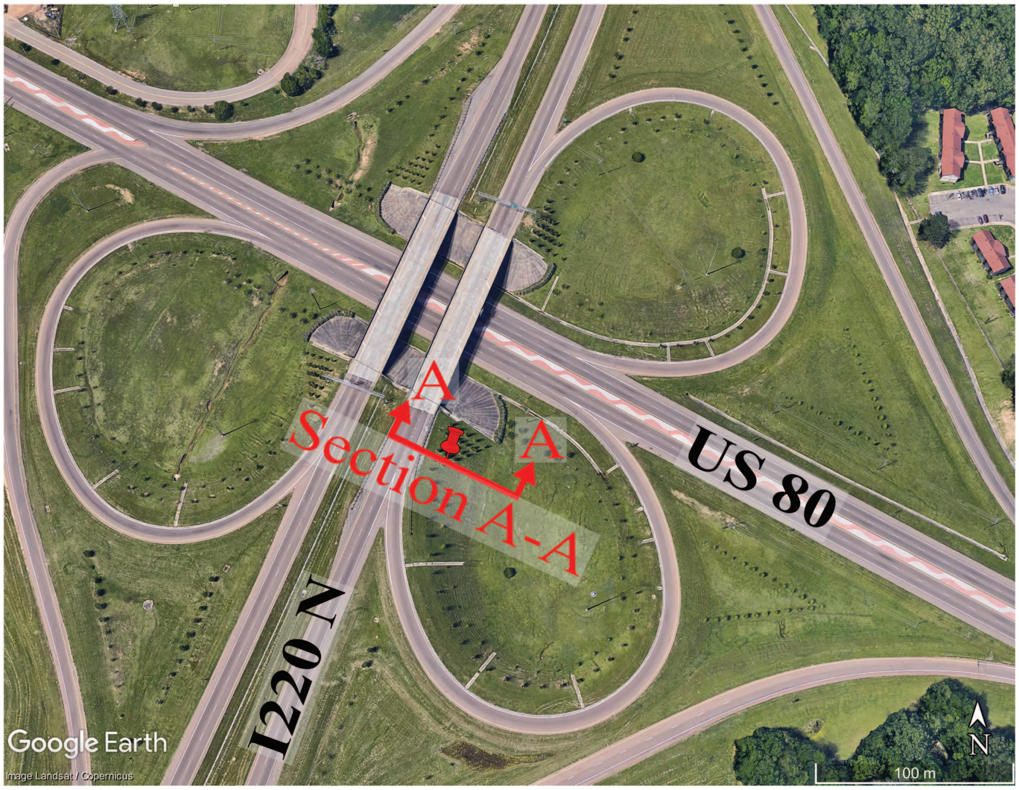

Fig. 1. (Color) Satellite image showing the site location. (Image © Google, image Landsat/Copernicus.)

Nat. Hazards Rev., 2025, 26(4): 04025052

Downloaded from ascelibrary.org by University of South Carolina on 08/20/25. Copyright ASCE. For personal use only; all rights reserved.

Downloaded from ascelibrary.org by University of South Carolina on 08/20/25. Copyright ASCE. For personal use only; all rights reserved.

Table 1. Magnitudes of different shear strength states of Yazoo clay

Parameter	Name	Unit	Residual strength	Fully softened	Unweathered
Effective cohesion	c'	kPa	4.8	8.7	143
Effective friction angle	ϕ'	Degrees	12.8	18.6	20

shown in Table 1. Additionally, all three clay layers have a hydraulic conductivity of 5.5×10^{-9} m/s and saturated unit weight of 21 kN/M^3. The site investigation determined the mean groundwater depth to be 4 m.

Methodology

The methodology comprises several steps, as illustrated in a methodological framework in Fig. 2. The process begins with creating a two-dimensional (2D) finite-element model of the embankment, calibrated using site data, slope geometry, and material properties. Preliminary analyses are then conducted to identify significant variables affecting the seepage and slope stability. The magnitudes for rainfall characteristics are extracted from intensity-duration-frequency curves. Next, the uncertainty in the occurrence of these variables is transformed into probability density functions. A total of 2,000 inputs are generated as part of the Monte Carlo simulation. Seepage and slope stability analyses are conducted for each set of these inputs. Concurrently, three limit states are defined. The input rainfall depth range is divided into several intervals, and the corresponding failure probability is calculated based on the output factor of safety (FoS) at each interval. Lognormal cumulative distribution functions are fitted to the failure probability data from the intervals using the maximum likelihood estimation. Finally, analytical fragility curves for three limit states are obtained.

Modeling Seepage and Slope Stability

The 2D highway embankment model is subjected to seepage and pore-water pressure change throughout the domain. The seepage calculation in a porous medium is based on Darcy's law, where fluid movement occurs due to hydraulic gradient. The corresponding 2D transient flow equation is expressed as follows:

$$\frac{\partial}{\partial x}\left(K_x \frac{\partial H}{\partial x}\right) + \frac{\partial}{\partial y}\left(K_y \frac{\partial H}{\partial y}\right) + Q' = \frac{\partial \theta}{\partial t} \qquad (1)$$

where K_x and K_y = are the hydraulic conductivities in the x- and y-directions; H = is the total head; Q' = is the boundary flux; and θ = is the volumetric water content, and t is the time.

The volumetric water content and hydraulic conductivity in partially saturated soil are formulated using van Genuchten's method (van Genuchten 1980). The volumetric water content as a function of pore-water pressure and soil water characteristic curve measures is given by

$$\theta = \theta_r + \frac{\theta_s - \theta_r}{[1 + (\frac{\psi}{\alpha})^n]^m} \qquad (2)$$

where θ_s = is the saturated volumetric water content; θ_r = is the residual volumetric water content; ψ is the negative pore-water pressure (matric suction); α approximately corresponds to inverse of air-entry value; and m and n are measures of pore size distribution. Similarly, the hydraulic conductivity K for changing pore-water pressure is formulated as

$$K = K_s \frac{[1 - (\alpha\psi^{(n-1)})(1 + (\alpha\psi^n)^{-m})]^2}{(((1 + \alpha\psi)^n)^{\frac{m}{2}})} \qquad (3)$$

where K_s is the saturated hydraulic conductivity.

The finite-element solution of this physical process is implemented in the SEEP/W module of GeoStudio software. The soil water characteristic curve of Yazoo clay used in this study is obtained from the laboratory test of Nobahar et al. (2019) and presented in Fig. 3. It is based on the laboratory test of the site soil samples, published in Nobahar et al. (2019). The given soil water characteristic curve is implemented in SEEP/W to calculate partially saturated soil parameters as a function of matric suction. These parameters are volumetric water content, hydraulic conductivity, and unit weight of the soil at partially saturated conditions. In the case of rainfall infiltration, the volumetric water content of the soil layer increases, resulting in increased unit weight and hydraulic conductivity.

The boundary conditions consist of rainfall as a hydraulic flux and groundwater depth as a hydraulic head function. The transient analysis, spanning 10 days, is divided into exponentially increasing time steps to capture short- and long-duration rainfalls with a successful numerical convergence. The seepage solution reflects the

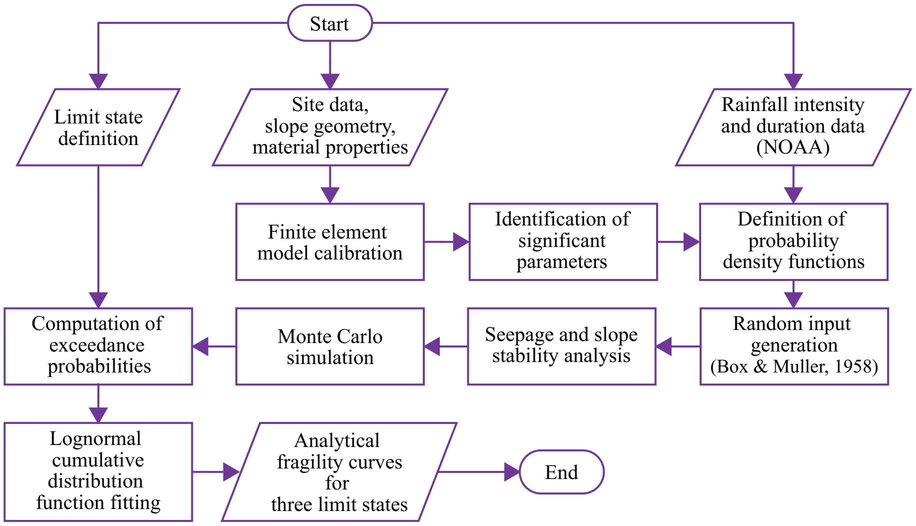

Fig. 2. (Color) Methodological framework.

Downloaded from ascelibrary.org by University of South Carolina on 08/20/25. Copyright ASCE. For personal use only; all rights reserved.

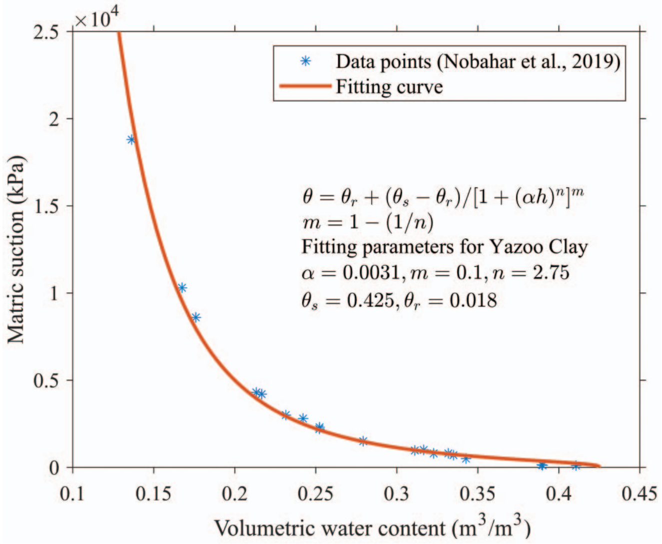

Fig. 3. (Color) Soilwater characteristic curve for Yazoo clay. (Data from Nobahar et al. 2019.)

increase in saturation of the top-level soil regions during the rainfall and the subsequent decrease once the rainfall ends. This increase in saturation results in heavier soil weight and reduced shear strength, thus inclining the slope toward failure. The degree of this tendency, i.e., FoS, is formulated based on Morgenstern-Price's method, based on the limit equilibrium, where the domain is divided into slices, in which the equilibrium conditions are formulated as

$$F_f = \frac{\sum(c'\beta\cos a + (N - u\beta)\tan\phi'\cos a)}{\sum N\sin a - \sum P\cos\omega} \tag{4}$$

$$F_m = \frac{\sum(c'\beta R + (N - u\beta)R\tan\phi')}{\sum Wx - \sum Nf \pm \sum Pd} \tag{5}$$

where F_f and F_m are the factors of safety equations with respect to the force equilibrium and moment equilibrium, respectively; c' is the effective cohesion; ϕ' is the effective friction angle; u is the pore-water pressure; N is the slice base normal force; W is the slice weight; P is the concentrated point load; a is the inclination of slice base; β is the slice base length; R is the radius of circular slip surface; x is the horizontal distance from slice centerline to the center of moments; f is the perpendicular offset of the normal force; d is the perpendicular distance from a point load to the center of moments; and ω is the angle of the point load.

The iterative process of identifying the most critical slide is conducted using the SLOPE/W module. The Mohr-Coulomb material model is employed for slope stability. The analysis results are assessed to be independent of variations in mesh size (1 m, 1.5 m, and 2 m). Accordingly, a mesh size of 1.5 m is selected for further analyses to optimize the balance between computational efficiency and the granularity needed for accurate analysis. This mesh size effectively partitions the upper 3-m-thick soil layers into two even sections, improving resolution where most critical, while also simplifying the computational model for the predominantly unweathered Yazoo clay in the lower layer. The domain is divided into 1,026 elements with 1,098 nodes.

Model Calibration

The field instrumentation data include time-dependent volumetric water content and matric suction measurements from moisture sensors located at the slope's crest, middle, and toe. For each of these locations, there are three sensors at depths of 1.5 m, 3 m, and 5 m. In addition, hourly rainfall data from site gauges covering 144 days between August 30, 2018, and January 21, 2019, are available. During this interval, the top-soil layers were in nearly saturated condition, leading to negligible changes in volumetric water content post-rainfall events. This condition likely occurs in Yazoo clay embankments due to their low hydraulic conductivity and tendency to retain infiltrated rainfall for extended durations.

On the other hand, the finite-element model is calibrated based on partially saturated conditions, allowing the display of the changes in volumetric water content resulting from rainfall infiltration. The boundary conditions consist of impermeable layers on the sides and the bottom, rainfall infiltration on the top, and the water head at the right side of the slope. This water head boundary condition represents the groundwater depth in the model (GEO-Slope International 2012). Fig. 4 presents the model geometry, locations of the nine sensors, and assigned layers. The top layer is composed of clay at its residual shear strength due to the presence of highly plastic clay susceptible to shrinkage and swelling resulting from seasonal wet-dry cycles (Khan et al. 2017). The middle layer of fully softened clay transitions between the active and unweathered zones.

The volumetric water content data from the nine sensors in the field are time-averaged to discard the fluctuations. Nine corresponding nodes are placed at the same locations in the finite-element model's mesh structure. The initial volumetric water content values at these nodes are manually adjusted by the groundwater depth

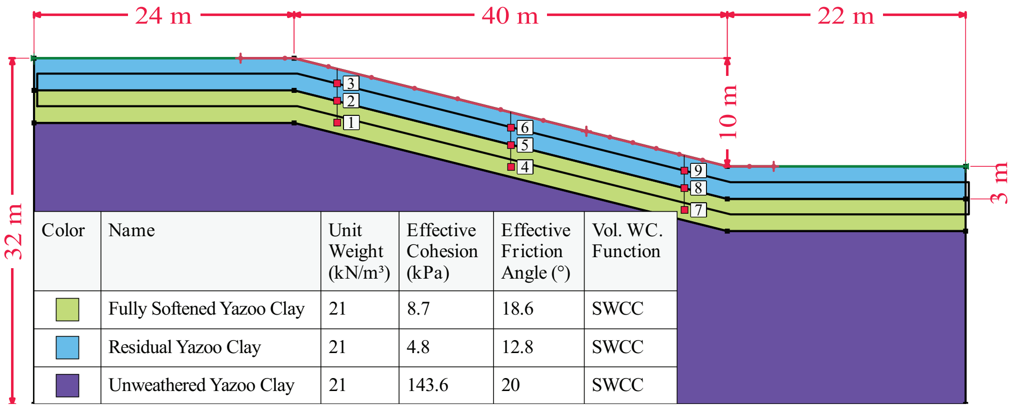

Color	Name	Unit Weight (kN/m³)	Effective Cohesion (kPa)	Effective Friction Angle (°)	Vol. WC. Function
🟩	Fully Softened Yazoo Clay	21	8.7	18.6	SWCC
🟦	Residual Yazoo Clay	21	4.8	12.8	SWCC
🟪	Unweathered Yazoo Clay	21	143.6	20	SWCC

Fig. 4. (Color) Two-dimensional finite-element model of Section A-A.

Downloaded from ascelibrary.org by University of South Carolina on 08/20/25. Copyright ASCE. For personal use only; all rights reserved.

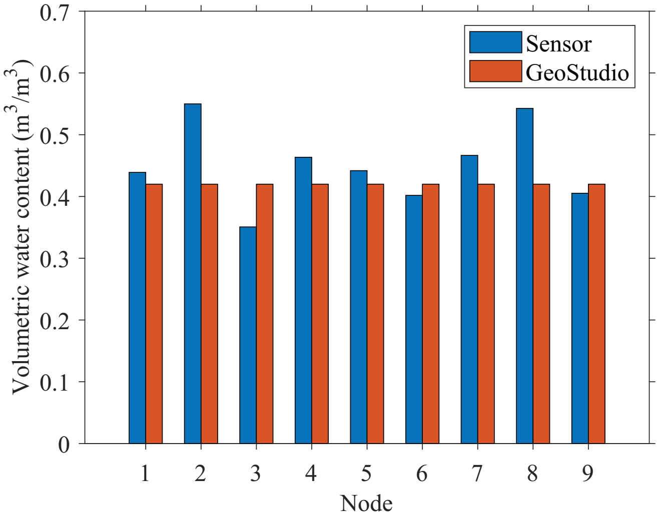

Fig. 5. (Color) Comparison of volumetric water content from the sensors and finite-element model.

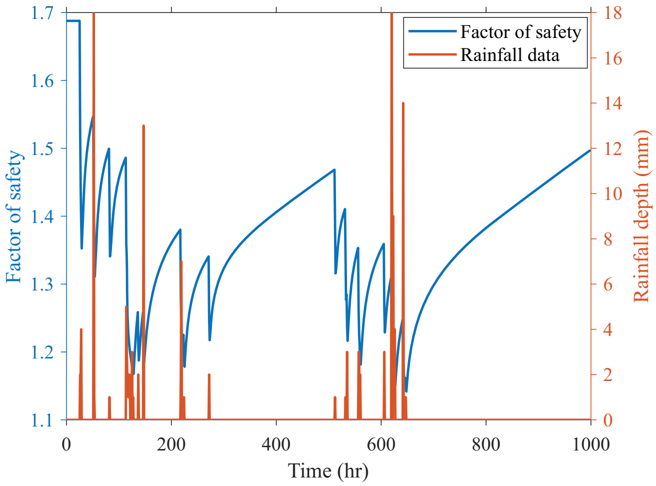

Fig. 6. (Color) Results of slope stability analysis for the site rainfall measurements.

to approximately match the sensor data. The volumetric water content values from the sensors and the model are presented in Fig. 5. These values reflect the initial conditions of the finite-element model prior to examining any rainfall effects.

The model's response to different rainfall characteristics was tested. The observed model results matched the predicted infiltration and rebound trends after the rainfall. Fig. 6 shows the slope stability analysis results of the model in response to the rainfall data over a 40-day period. The rainfall intensity is calculated by assuming that these events are uniformly distributed throughout each hour. These individual rainfall events are not extreme in magnitude and are typical for the season. However, given the nearly saturated conditions of the soil prior to the recorded data period, it is evident that successive rainfall events cumulatively reduce the FoS. This gradual reduction in FoS can lead to increasingly susceptible conditions for slope failure, particularly in scenarios where the soil remains saturated over prolonged periods, diminishing its capacity to absorb additional water effectively. Fig. 6 shows that the changes in the FoS are very rapid, which is due to the soil-water characteristic curve of Yazoo clay. The varying volumetric water content significantly affects matric suction, resulting in sudden changes in shear strength parameters. In Fig. 3, the vertical axis is scaled by a factor of 10^4. This highlights how small shifts in volumetric water content can cause remarkable changes in matric suction for this soil type.

Table 2. Precipitation frequency estimates (in mm/h)

		Return period (years)				
Rainfall category	Duration	50	100	200	500	1,000
High-intensity and short-duration	30-min	129	142	155	173	186
Medium-intensity and medium-duration	6-h	27	30	34	39	43
Low-intensity and long-duration	3-day	3	4	4	5	5
	7-day	1	2	2	2	3

Description of the Selected Rainfall Characteristics and Groundwater Depth

Preliminary analyses are conducted to identify the essential variables influencing the rainfall-induced slope stability of highway embankments. The results suggest that the rainfall intensity, rainfall duration, and groundwater depth prior to rainfall play important roles in affecting the saturation and the resultant FoS of the slope. Consequently, the effects of any variations in the magnitudes of these variables are inspected.

To develop fragility curves that reflect a wide range of rainfall conditions, encompassing both short and long durations, the following durations were selected as representative categories of shorter to longer durations: 30-min, 6-h, 3-day, and 7-day. The corresponding intensities are determined using the intensity-duration-frequency curves. These four characteristics are categorized into high-intensity and short-duration, medium-intensity and medium-duration, and low-intensity and long-duration. It should be noted that the low-intensity and long-duration rainfall category includes both 3- and 7-day durations. The decision to combine these two durations is made based on the insights both durations provide. Table 2 presents the employed intensity-duration-frequency magnitudes for different return periods. The uncertainty in the rainfall durations is captured by assigning probability density functions with a mean value equal to the selected duration within a range of ±25% deviations from the mean. Similarly, the uncertainty in the rainfall intensities is reflected by corresponding probability density functions. In these cases, the mean values correspond to a return period of 200 years, while the range spans return periods between 50 years and 1,000 years. It should be noted that the occurrence of 7-day rainfall is rare; however, including these events in the analysis extends the range of rainfall depths that the fragility curve can cover.

Greater return period events for each rainfall category resulted in an increase in the total rainfall depth, leading to greater infiltration and saturation. This situation results in a more pronounced reduction in the FoS, thereby increasing the tendency of slope failure. Generally, highway embankment slopes are designed to withstand rainfall events up to a 50-year return period. It might be extended to a 100-year return period for more critical locations. However, ongoing climate change is altering the frequency and intensity of these return period events. The more frequent occurrence of high return period events does not allow enough rebound time for the slope to recover from one significant rainfall event before being hit by the next. Therefore, the nearly saturated conditions are more likely to occur due to climate change. Additionally, increased intensities result in more substantial total rainfall for the same duration, leading to higher saturation levels and lower corresponding FoS values.

Nat. Hazards Rev., 2025, 26(4): 04025052

Downloaded from ascelibrary.org by University of South Carolina on 08/20/25. Copyright ASCE. For personal use only; all rights reserved.

This study models the slope under higher–return period events, i.e., a mean of 200-year return period rainfall intensity. Regarding the increased frequency of extreme rainfalls, the variation of initial conditions is captured by introducing random groundwater levels in the model to reflect the potential effects of preceding extreme weather events. For instance, a simulation with an initial groundwater depth set at 3 m might simulate conditions following a recent heavy rain, while starting with a depth of around 5 m could represent a drier period. Based on the defined probability density function, this method more frequently generates groundwater depths around the mean of 4 m while less often producing values near 3-m and 5-m extremes. This approach accounts for the likelihood of different initial conditions due to varying weather patterns prior to the analyzed rainfall event.

Fragility Curves

Rainfall characteristics vary spatially and temporally. Similarly, the embankment slope may experience varying groundwater depths and, thus, different matric suction profiles. The combination of uncertainties in both the load and resistance of the structure brings a comprehensive understanding of the effects of rainfall on slope stability. Uncertainties in such parameters are considered through Monte Carlo simulation analysis, which enables the generation of a range of potential rainfall scenarios, each with an associated likelihood. It should be noted that the uncertainties in the soil shear strength parameters, c' and ϕ', in Eqs. (4) and (5), are disregarded. Their variation around the mean value might cause higher or lower FoS. However, their magnitudes are assumed to be constant to focus solely on the impact of rainfall and corresponding seepage on stability.

For the Monte Carlo simulation, the three uncertain parameters, namely rainfall intensity, rainfall duration, and groundwater depth, are assumed to be normally distributed variables. Table 3 provides these distributions' mean, lower, and upper limits. For each rainfall category, the limits of intensity (i) and durations (t), as well as the corresponding rainfall depths (RD), are given. Some rainfall depths intersect across different rainfall categories, illustrating that various intensity and duration combinations can yield the same total rainfall. However, their effects on the slope differ due to the different rates affecting infiltration velocities and capacities. The high-intensity and short-duration rainfalls result in relatively more minor total rainfall depth than lower intensity and longer duration events.

Table 3. The mean and limits of the normally distributed variables

Variables	Name	Lower limit	Mean	Upper limit
High-intensity and short-duration rainfall	i_{hs} (mm/h)	129	155	186
	t_{hs} (min)	22	30	38
	RD_{hs} (mm)	47.3	77.5	117.8
Medium-intensity and medium-duration rainfall	i_{mm} (mm/h)	27	34	43
	t_{mm} (h)	4.5	6	7.5
	RD_{mm} (mm)	121.5	204	322.5
Low-intensity and long-duration rainfall (1)	i^1_{ll} (mm/h)	3	4	5
	t^1_{ll} (days)	2.25	3	3.75
	RD^1_{ll} (mm)	162	288	450
Low-intensity and long-duration rainfall (2)	i^2_{ll} (mm/h)	1	2	3
	t^2_{ll} (days)	5.25	7	8.75
	RD^2_{ll} (mm)	126	336	630
Groundwater depth	d (m)	3	4	5

The Box–Muller transformation method, known for its wide usage in the literature, was used for generating samples from a normal distribution (Box and Muller 1958). Figs. 7(a–h) show the histograms of generated samples for each rainfall variable. Their approximate forms of normal probability density functions are demonstrated. Monte Carlo simulation realizations are formed from pairs of randomly generated rainfall intensities and durations specific to each rainfall category based on the depicted values in intensity-duration-frequency curves. For instance, Fig. 8 illustrates the Monte Carlo simulation inputs for high-intensity, short-duration rainfall events. These pairs create a rectangular hyetograph, which is applied to the finite-element model as a boundary condition. Each color in the figure represents a different realization, corresponding to an input depicted in Fig. 7(a). While both intensity and duration realizations fall within the limits specified in Table 3, the most frequently applied magnitudes tend to be the mean values of 155 mm/h and 0.5 h, respectively. Similar hyetographs are generated for each rainfall category, allowing a diverse range of rainfall scenarios to be represented and analyzed.

Monte Carlo simulation is conducted using GeoStudio's SEEP/W and SLOPE/W modules. A Visual Basic script is developed in Visual Studio to automate the execution of the analyses. Each transient analysis consists of a time-dependent FoS output; thus, the minimum value is recorded to account for the most severe time instances. There are 2,000 analyses conducted for Monte Carlo simulation, with 500 simulations allocated to each of the four rainfall categories. The selection of 2,000 samples aims at optimizing the balance between computational time and the quality of results. While a larger sample size tends to smooth the resultant histograms and enhances the subsequent fragility curve fitting, it extends the total duration of the Monte Carlo simulation. The adequacy of this sample size is affirmed as the fitted fragility curves pass the Lilliefors goodness-of-fit test, demonstrating that the sample size was sufficient to develop robust and reliable fragility curves.

The embankment slope stability guidelines are well documented by the U.S. Army Corps of Engineers (USACE 2021); typical minimum design FoS values are 1.5 for normal long-term loading conditions and 1.1 to 1.3 for infrequent loading conditions. Accordingly, three different limit states are defined for this study. The minor limit state is defined as any FoS below 1.5, indicating that while the slope remains within acceptable conditions, it is nearing the lower threshold of design safety. A further limit state, termed "medium," is bounded by the FoS of 1.3; any FoS below this threshold suggests that the safety of the slope is starting to become compromised. The most severe limit state, "major," is specified at FoS of 1.1. A slope reaching this FoS in response to a rainfall event is considered risky, which warrants precautionary measures. The safety margin between the designed FoS of 1.5 and the deterministic failure point of FoS 1 is segmented into these three distinct limit states, effectively grading the severity of the conditions. The three limit states, LS, are defined as follows:

$$LS(\text{FoS}) = \begin{cases} \text{"Major"} & \text{when FoS} \leq 1.1 \\ \text{"Medium"} & \text{when FoS} \leq 1.3 \\ \text{"Minor"} & \text{when FoS} \leq 1.5 \end{cases} \tag{6}$$

It is worth noting that when the FoS dropped below the critical value, it exceeded the defined limit states. This failure does not necessarily reflect a physical failure at the site, but it indicates that the structure's capacity to provide a specified level of service has been exceeded. The direct damage from the rainfall load is the increased saturation level of the domain, which is the early indicator of failure. As the saturation level rises, the slope's strength diminishes, directly

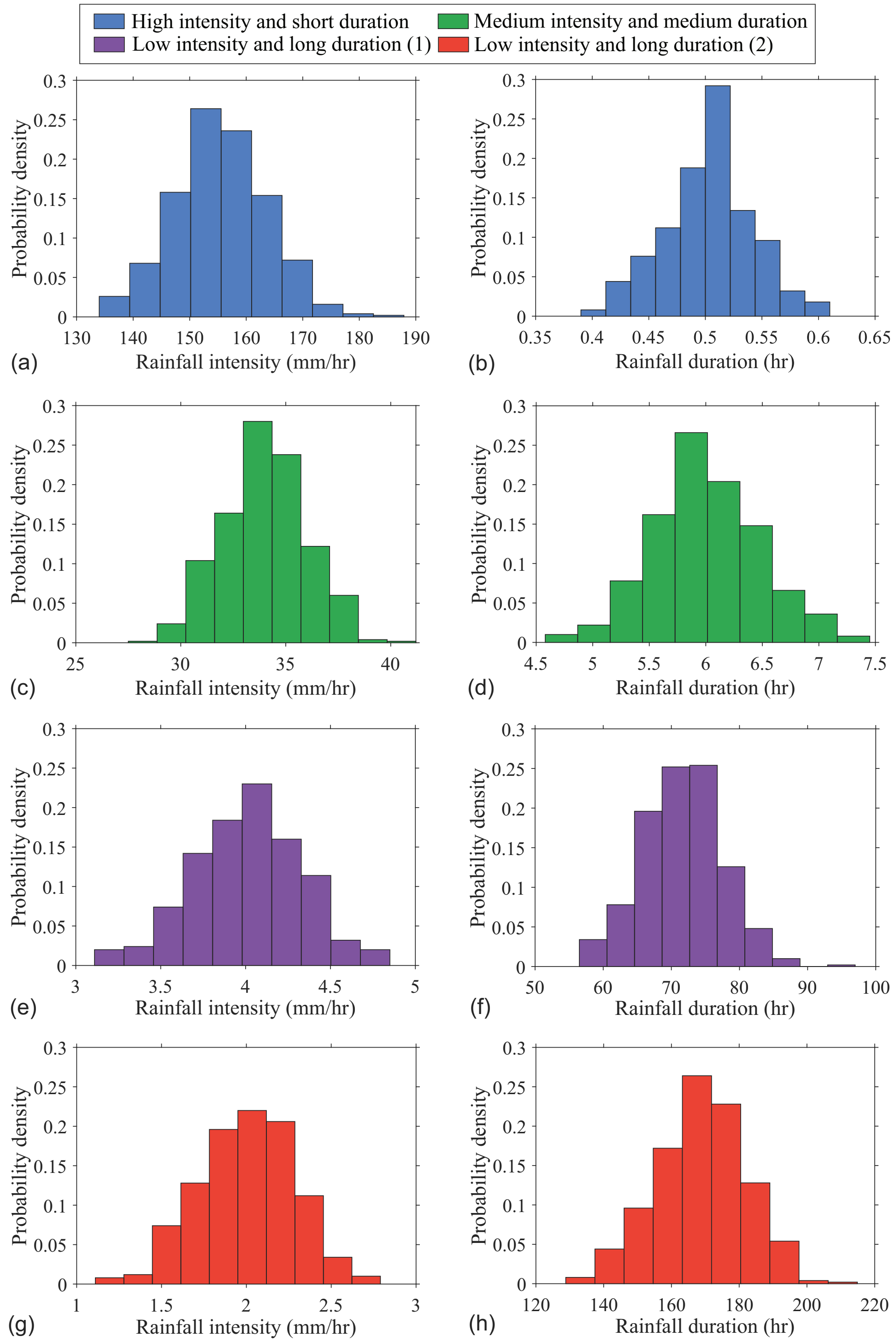

Fig. 7. (Color) Histograms of input boundary conditions.

reducing the FoS both during and immediately after the rainfall and making it more vulnerable to future rainfall events.

Fragility curves are developed for the three limit states based on the results of the Monte Carlo simulation outcome using the maximum likelihood estimation (Shinozuka et al. 2000a, b, 2002; Dang et al. 2017). The maximum likelihood estimation method allows the estimation of the characteristics of the probability distribution that make the observed data most probable. This is achieved by defining an objective function that quantifies the deviation between the observed data and the theoretical distribution and numerically optimizing this function to find the parameters that minimize this deviation. A lognormal distribution is assumed for the three fragility curves, as customary in the literature (e.g., Singhal and Kiremidjian 1996; Shinozuka et al. 2000b; Ellingwood et al. 2004, 2007; Ellingwood 2008; Casciati et al. 2008; Baker 2015). Additionally, a lognormal distribution is preferable for modeling the fragility curves because it restricts intensity measures to positive values. This characteristic aligns with the physical realities in civil engineering,

Downloaded from ascelibrary.org by University of South Carolina on 08/20/25. Copyright ASCE. For personal use only; all rights reserved.

Downloaded from ascelibrary.org by University of South Carolina on 08/20/25. Copyright ASCE. For personal use only; all rights reserved.

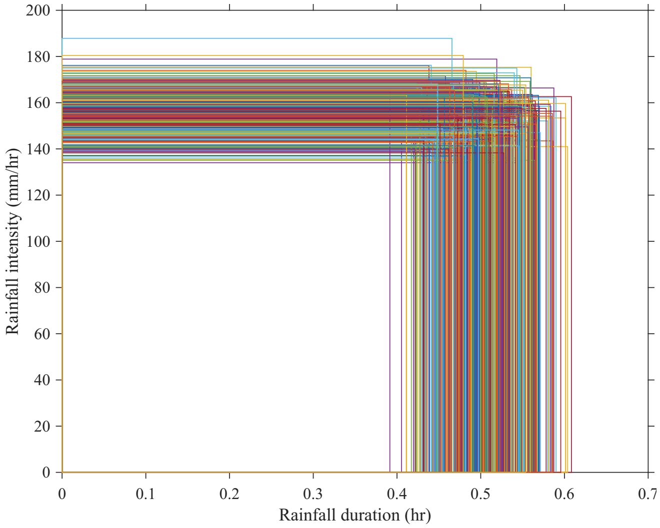

Fig. 8. (Color) Randomly generated hyetograph input for high-intensity and short-duration rainfalls.

where such measures inherently cannot be negative. The fragility curve, $F_r(r)$, representing the conditional probability of exceeding a limit state, $P(LS \geq ls|RD = r)$ can be expressed as

$$F_r(r) = P(LS \geq ls|RD = r) \tag{7}$$

where $P(LS \geq ls|RD = r)$ is the probability that the FoS falling below a specific limit state threshold ls when the rainfall depth (e.g., intensity measure), RD, is equal to a certain rainfall depth, r. This probability reflects the fragility function in the form of a lognormal cumulative distribution function with a median, θ', and standard deviation, β':

$$P(LS \geq ls|RD = r) = \Phi\left(\frac{\ln(r/\theta')}{\beta'}\right) \tag{8}$$

where Φ is the standard normal cumulative distribution function.

For a lognormal distribution, the likelihood function, $L(\theta', \beta')$, is the product of the individual probabilities given by the cumulative distribution function:

$$L(\theta', \beta') = \prod_{i=1}^{N} [F_r(r_i; \theta', \beta')]^{Y_i} [1 - F_r(r_i; \theta', \beta')]^{1-Y_i} \tag{9}$$

where N is the number of intervals the rainfall depth range is divided into, r_i is the rainfall depth from each interval center, and Y_i is a Bernoulli random variable and is equal to $Y_i = 1$ if a limit state is exceeded; if not, $Y_i = 0$. The natural logarithm of the likelihood function, log-likelihood, ll, is taken to turn the product terms into sums:

$$ll(\theta', \beta') = \sum_{i=1}^{n} Y_i \cdot \ln[F_r(r_i; \theta', \beta')] + (1 - Y_i) \cdot \ln[1 - F_r(r_i; \theta', \beta')] \tag{10}$$

Next, the maximization of the likelihood function is to be performed. Considering the numerical optimization methods are mainly designed to minimize functions, the log-likelihood equation is multiplied by −1 to obtain the negative log-likelihood function, nll, as follows:

$$\text{nll}(\theta', \beta') = -\sum_{i=1}^{n} Y_i \cdot \ln[F_r(r_i; \theta', \beta')] + (1 - Y_i) \cdot \ln[1 - F_r(r_i; \theta', \beta')] \tag{11}$$

The optimization problem results in the following minimization of the negative log-likelihood function:

$$(\hat{\theta}', \hat{\beta}') = \arg\min_{\theta', \beta'}(\text{nll}(\theta', \beta')) \tag{12}$$

The estimated lognormal cumulative distribution function parameters, $(\hat{\theta}', \hat{\beta}')$, are calculated following the aforementioned steps. It should be noted that, although maximum likelihood estimation is common in the literature, this method has certain inherent limitations (e.g., Ioannou et al. 2012; Mai et al. 2017; Zentner et al. 2017; Rohmer et al. 2020) and alternative methods can be employed for different applications.

Results and Discussion

Transient analysis results typically reveal a certain general behavior in the seepage and slope stability models during rainfall events. In particular, the infiltration causes the phreatic surface to rise toward the top layer during the rainfall. During this stage, the FoS of the slope significantly decreases, reaching its minimum value at the end of the rainfall. Similarly, when the rainfall stops, the phreatic surface descends to deeper depths, and FoS increases.

This model behavior is presented in Fig. 9 for a 3-day-long rainfall event from the low-intensity and long-duration rainfall category. Fig. 9(a) shows the initial matric suction distribution across the domain, and the corresponding FoS is 1.69 on Day 0. The impact of the rainfall is the increased pore-water pressure of top layers in Fig. 9(b) on Day 3 when the rain stops. It is observed that the model domain is almost fully saturated, and the FoS has reached its minimum with a 33% reduction from the initial value. Finally, Fig. 9(c) depicts the result on Day 30. It shows that the initial matric suction distribution and the corresponding FoS are restored to the initial distribution again on Day 30. This demonstrates a considerably long rebound period of upper clay layers and indicates the increased severity of saturation during consecutive rainfall events. In other words, after the representative 3-day-long rainfall, any successive rainfall within 30 days would accelerate the fully saturated conditions conducive to more severe damage to the slope.

The rise of the phreatic surface is relatively faster for high-intensity and short-duration rainfalls but with a minor overall increase in height. This quick response reflects the sudden but limited total infiltration, as the short rainfall duration does not allow for extensive saturation of the upper soil layers, resulting in a relatively minor reduction in the FoS. Conversely, low-intensity and long-duration rainfall events lead to a slower but more significant rise in the phreatic surface, resulting in almost fully saturated top-soil layers. This gradual process increases the soil weight, leading to substantially lower FoS values. Medium-intensity and medium-duration rainfalls deliver a middle ground between total rainfall depths and saturation from the aforementioned two extremes of rainfall categories.

The histograms of output FoS for each rainfall category are plotted in Figs. 10(a–d). These results reveal that the FoS distribution for each rainfall category approximately follows a normal distribution. In examining these histograms, it is apparent that the mean FoS decreases from high-intensity and short-duration to low-intensity and long-duration rainfalls. This suggests that the low-intensity and long-duration rainfalls cause more severe damage to highway

Downloaded from ascelibrary.org by University of South Carolina on 08/20/25. Copyright ASCE. For personal use only; all rights reserved.

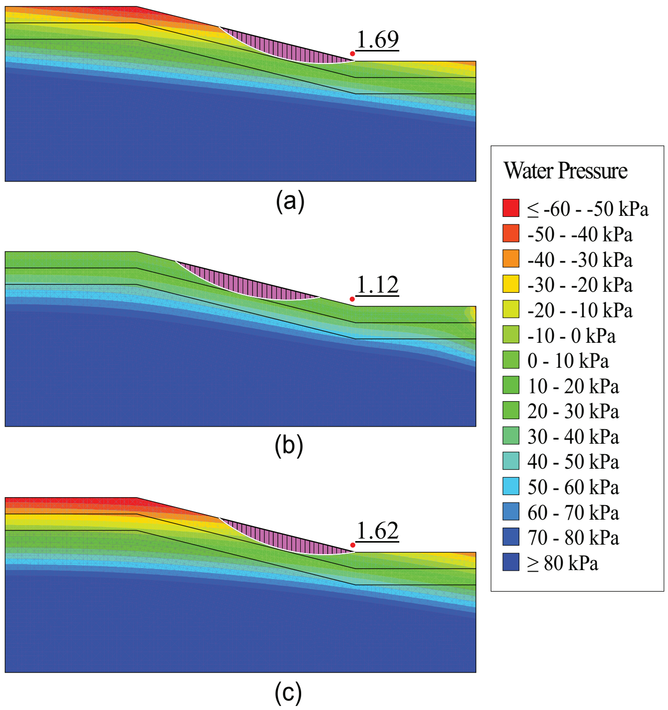

Fig. 9. (Color) Model behavior during the 3-day-long rainfall: (a) initial conditions on Day 0; (b) highly saturated top layers when the rainfall stops on Day 3; and (c) restored initial conditions on Day 30.

embankment slopes with a mean FoS of 1.087 after a 7-day rainfall [see Fig. 10(d)]. It should be noted that this 7-day rainfall has a mean intensity of 2 mm/h.

This observation agrees with the understanding that a soil's infiltration capacity is limited by its hydraulic conductivity, and the excess rain becomes surface runoff. Therefore, the rainfall duration appears to be the most significant factor in slope stability. Increasing duration exposes upper soil layers to longer infiltration time, thus creating a more saturated ground that is more prone to failure. On the other hand, high-intensity and short-duration rainfall events cause less damage in terms of slope stability. The limited absorption time for the soil results in most of the rainfall depth shifting to surface runoff.

Notably, the lowest FoS recorded is approximately 1.077 [as depicted in Fig. 10(d)] under the most severe rainfall conditions. This critical state typically arises when high groundwater levels, i.e., nearly saturated upper soil layers, couple with a long-duration rainfall. The same rainfall event might yield a higher FoS if coupled with a lower groundwater level. This underscores the importance of considering the probabilistic combinations of rainfall events and pre-rainfall groundwater levels in Monte Carlo simulations for a comprehensive slope stability analysis. Furthermore, this minimum FoS represents a small fraction of the overall probability density function, indicating a lower likelihood of occurrence.

The most severe FoS values for the first three rainfall categories are 1.42, 1.22, and 1.11, respectively. These findings imply that the current slope configuration remains above the traditional failure criterion of FoS less than 1. However, this conclusion takes only the uncertainty in rainfall characteristics and groundwater depth into account. If uncertainties in soil shear strength parameters were also considered, potentially even lower FoS values might be observed.

The validity of the developed fragility curves is assessed using the Lilliefors goodness-of-fit test as described in Porter et al. (2006, 2007). The curves are tested at the 5% significance level, i.e., the proposed lognormal distribution curves are assessed to be acceptable for a 95% confidence level. The maximum difference between the theoretical and empirical cumulative distributions, D, is calculated as 0.249, 0.048, and 0.134 for minor, medium, and major limit states, respectively. The recommended critical difference, D_{crit}, corresponding to the 5% significance level, is determined to be 0.291.

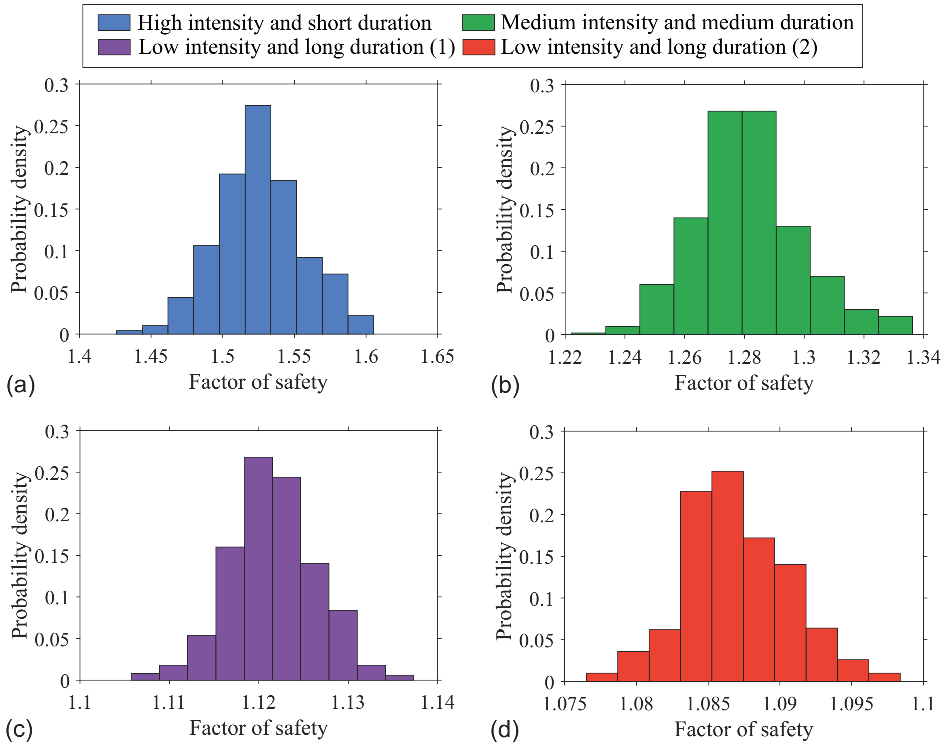

Fig. 10. (Color) Histograms of FoS (Monte Carlo simulation output) for each rainfall category.

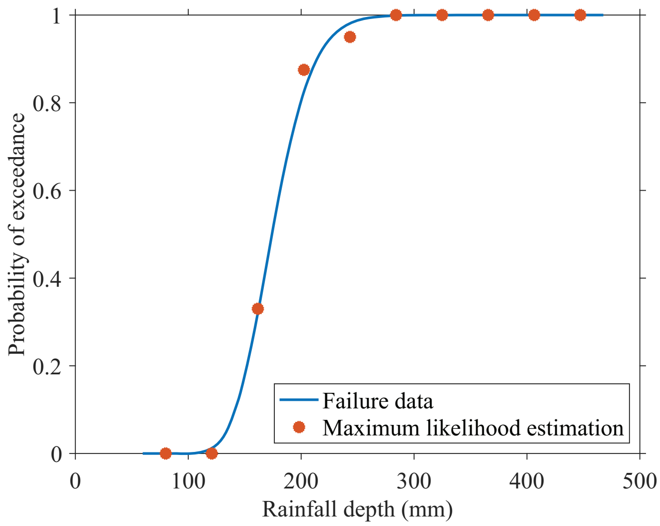

Fig. 11. (Color) Lognormal fragility curves based on maximum likelihood estimation for the medium limit state.

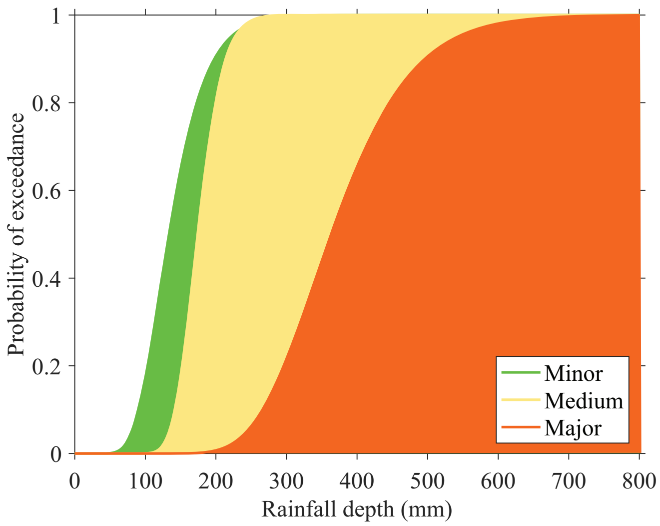

Fig. 12. (Color) Fragility curves for slope failure at different limit states.

Table 4. Median and standard deviation of the fragility curves

Limit states	Critical FoS	θ'	β'
Minor	1.5	133	0.31
Medium	1.3	174	0.16
Major	1.1	365	0.24

Since $D < D_{\text{crit}}$ for all three limit states, the goodness-of-fit of the developed fragility curves is accepted based on this common practice in the literature. Fig. 11 presents an estimated cumulative distribution function fit based on the maximum likelihood estimation. This is the output for the medium limit state, where the critical FoS is 1.3. It is visually supported that the lognormal cumulative distribution function, estimated using the failure data from each rainfall interval, corresponds closely with the calculated probability of exceedance.

Table 4 reports the θ' and β' parameters for the estimated lognormal curves. The median value, θ', corresponds to a rainfall depth with a 50% exceedance probability of a limit state. For example, a rainfall depth of 133 mm would result in a 50% probability of exceeding the minor limit state. These parameters can be used to reproduce the fragility curves and calculate the probability of exceedance for other rainfall depths.

The comprehensive fragility curves for three limit states are presented in Fig. 12. These curves represent the probability of exceeding a limit state for a wide range of potential rainfall depths. The plot covers the majority of the intensity-duration-frequency data to which the slope might be subjected throughout its service life. As observed, the exceedance of the major limit state is only possible for rainfall depths within the 200–650 mm range. On the other hand, even the minor limit state is not exceeded for rainfall depths below 65 mm.

Additionally, the figure suggests that exceeding the medium limit state is only possible for rainfall depths exceeding approximately 100 mm. The median value, i.e., 50% probability of exceedance, is 174 mm. Once rainfall depths exceed 230 mm, the exceedance probability reaches 95%. Similarly, the major limit state might be exceeded for post-200-mm rainfalls, with the probability reaching 95% for rainfalls of 550 mm or more.

The developed fragility curves can be used to assess the safety of similar slopes in the region. This plot could be used to evaluate suspected slope failure following a recent heavy rainfall event. Additionally, design engineers may utilize this plot in future designs of highway embankments. Considering that the rainfall input is based on extreme, higher–return period events, this plot can be adapted for design actions based on future extremes.

A limitation of applying the presented methodology to Yazoo clay is that the soil water characteristic curve has its upper and lower bounds due to the previously mentioned cracks in the soil resulting from wet-dry cycles. Current finite-element software does not allow for accounting for different bounds of the soil water characteristic curve. Therefore, this study used the average soil water characteristic curve for Yazoo clay, resulting in minor discrepancies between the sensor data and the finite-element model data.

Conclusion

The stability of highway embankments under extreme rainfall events has been investigated. An example site located in Jackson, Mississippi, with available soil parameters and matric suction data, is selected for this study. A finite-element model is developed and calibrated using the site data to simulate the impacts of different rainfall characteristics. Rainfall events are divided into four categories, considering their intensity and duration. The effects of extreme rainfalls are considered in two different ways: the increased mean rainfall intensity and changing groundwater depth related to the increased frequency of extreme events. Monte Carlo simulation is conducted using GeoStudio software. The seepage and slope stability analyses are performed, and the factor of safety against slope failure for each set of inputs is computed. Different limit states are established based on the recommended minimum acceptable factor of safety values in design guidelines. The simulation inputs and the corresponding outputs were utilized to construct fragility curves. Lognormal cumulative distribution functions are fitted to Monte Carlo simulation outputs using maximum likelihood estimation. The plot of continuous limit state exceedance probabilities of the highway embankment slope for a wide range of rainfall loads is presented. The following are key findings of this study:

Downloaded from ascelibrary.org by University of South Carolina on 08/20/25. Copyright ASCE. For personal use only; all rights reserved.

Downloaded from ascelibrary.org by University of South Carolina on 08/20/25. Copyright ASCE. For personal use only; all rights reserved.

- Highway embankment slopes are more susceptible to serious damage from low-intensity and long-duration rainfalls than higher intensity and shorter duration rainfalls.
- Rainfall duration emerges as the critical variable influencing the soil saturation level for the case considered here, thereby affecting the slope's vulnerability. This increased slope failure tendency is attributed to the low infiltration capacity characteristic of highly plastic soil types.
- The probability of exceeding each limit state increased proportionally to rainfall depths. This revealed the more severe impact of extreme rainfall intensity.
- The long rebound duration of Yazoo clay is demonstrated. Regarding the increased frequency of extreme rainfall events, the higher impact from consecutive rainfall events is revealed.
- The lowest computed FoS in this investigation is 1.07. This is lower than the required minimum FoS recommendations in embankment design guidelines.
- For any given rainfall depth, there are distinct probabilities that it will exceed various limit states, as demonstrated by the fragility curves. Therefore, a specific rainfall depth should not be directly linked to a particular damage outcome. Instead, each rainfall depth is associated with its own set of probabilities for causing different levels of damage.

The methodology is applicable for fragility curve building for different embankment types when considering slope stability. The framework mainly applies to regions with high-plasticity clay commonly used for embankment filling.

Data Availability Statement

Some or all data, models, or code that support the findings of this study are available from the corresponding author upon reasonable request.

Acknowledgments

The authors gratefully acknowledge the support of the National Science Foundation (Award No. 2152896).

Author Contributions

Ege Can Kurter: Conceptualization; Data curation; Investigation; Methodology; Software; Visualization; Writing – original draft; Writing – review and editing. Mohammad Sadik Khan: Conceptualization; Data curation; Funding acquisition; Methodology; Resources; Supervision; Writing – review and editing. Laura Micheli: Conceptualization; Formal analysis; Funding acquisition; Methodology; Supervision; Writing – review and editing. Austin R.J. Downey: Conceptualization; Funding acquisition; Supervision; Visualization. Jasim Imran: Conceptualization; Funding acquisition; Methodology; Project administration; Supervision; Writing – review and editing.

Notation

The following symbols are used in this paper:

a = inclination of slice base;
c' = cohesion;
D = difference between the theoretical and empirical cumulative distributions;
D_{crit} = critical difference in Lilliefors test;
d = perpendicular distance from a point load to the center of moments;
F_f = force equilibrium;
F_m = moment equilibrium;
F_r = fragility function;
f = perpendicular offset of the normal force;
H = total head;
i = rainfall intensity;
K_x = horizontal hydraulic conductivity;
K_y = vertical hydraulic conductivity;
L = likelihood function;
ll = log-likelihood function;
m, n = measures of pore size distribution in van Genuchten equation;
N = slice base normal force;
nll = negative log-likelihood function;
P = concentrated load;
Q' = boundary flux;
R = radius of circular slip surface;
RD = rainfall depth;
t = rainfall duration;
u = pore-water pressure;
W = slice weight;
x = horizontal distance from slice centerline to the center of moments;
α = van Genuchten equation parameter corresponding to the inverse of air-entry value;
β = slice base length;
β' = standard deviation;
$\hat{\beta}'$ = standard deviation estimation;
θ = volumetric water content;
θ' = median;
$\hat{\theta}'$ = median estimation;
θ_r = residual volumetric water content;
θ_s = saturated volumetric water content;
Φ = standard normal cumulative distribution function;
Φ' = friction angle;
ψ = matric suction; and
ω = angle of the point load.

References

Apel, H., A. H. Thieken, B. Merz, and G. Blöschl. 2006. "A probabilistic modelling system for assessing flood risks." *Nat. Hazard.* 38 (May): 79–100. https://doi.org/10.1007/s11069-005-8603-7.

Baker, J. W. 2015. "Efficient analytical fragility function fitting using dynamic structural analysis." *Earthquake Spectra* 31 (1): 579–599. https://doi.org/10.1193/021113EQS025M.

Box, G. E., and M. E. Muller. 1958. "A note on the generation of random normal deviates." *Ann. Math. Stat.* 29 (2): 610–611. https://doi.org/10.1214/aoms/1177706645.

Casciati, F., G. P. Cimellaro, and M. Domaneschi. 2008. "Seismic reliability of a cable-stayed bridge retrofitted with hysteretic devices." *Comput. Struct.* 86 (17–18): 1769–1781. https://doi.org/10.1016/j.compstruc.2008.01.012.

Celik, O. C., and B. R. Ellingwood. 2008. "Modeling beam-column joints in fragility assessment of gravity load designed reinforced concrete frames." *J. Earthquake Eng.* 12 (3): 357–381. https://doi.org/10.1080/13632460701457215.

Choi, E., R. DesRoches, and B. Nielson. 2004. "Seismic fragility of typical bridges in moderate seismic zones." *Eng. Struct.* 26 (2): 187–199. https://doi.org/10.1016/j.engstruct.2003.09.006.

Downloaded from ascelibrary.org by University of South Carolina on 08/20/25. Copyright ASCE. For personal use only; all rights reserved.

Dang, C.-T., T.-P. Le, and P. Ray. 2017. "A novel method based on maximum likelihood estimation for the construction of seismic fragility curves using numerical simulations." *C. R. Méc.* 345 (10): 678–689. https://doi.org/10.1016/j.crme.2017.06.011.

D'Oria, M., A. Maranzoni, and M. Mazzoleni. 2019. "Probabilistic assessment of flood hazard due to levee breaches using fragility functions." *Water Resour. Res.* 55 (11): 8740–8764. https://doi.org/10.1029/2019WR025369.

Ellingwood, B. R. 2008. "Structural reliability and performance-based engineering." *Proc. Inst. Civ. Eng. Struct. Build.* 161 (4): 199–207. https://doi.org/10.1680/stbu.2008.161.4.199.

Ellingwood, B. R., O. C. Celik, and K. Kinali. 2007. "Fragility assessment of building structural systems in Mid-America." *Earthquake Eng. Struct. Dyn.* 36 (13): 1935–1952. https://doi.org/10.1002/eqe.693.

Ellingwood, B. R., D. V. Rosowsky, Y. Li, and J. H. Kim. 2004. "Fragility assessment of light-frame wood construction subjected to wind and earthquake hazards." *J. Struct. Eng.* 130 (12): 1921–1930. https://doi.org/10.1061/(ASCE)0733-9445(2004)130:12(1921).

GEO-Slope International. 2012. *Seepage modeling with SEEP/W.* Calgary, AB, Canada: GEO-Slope International.

Hall, J. W., R. Dawson, P. Sayers, C. Rosu, J. Chatterton, and R. Deakin. 2003. "A methodology for national-scale flood risk assessment." In Vol. 156 of *Proc., Institution of Civil Engineers-Water and Maritime Engineering*, 235–247. London: Thomas Telford.

Ioannou, I., T. Rossetto, and D. Grant. 2012. "Use of regression analysis for the construction of empirical fragility curves." In *Proc., 15th World Conf. on Earthquake Engineering*. Lisbon, Portugal: Sociedade Portuguesa de Engenharia Sismica.

Jasim, F. H., F. Vahedifard, E. Ragno, A. AghaKouchak, and G. Ellithy. 2017. "Effects of climate change on fragility curves of earthen levees subjected to extreme precipitations." In *Geo-Risk 2017*, 498–507. Reston, VA: ASCE.

Khan, M. S., S. Hossain, A. Ahmed, and M. Faysal. 2017. "Investigation of a shallow slope failure on expansive clay in Texas." *Eng. Geol.* 219 (Mar): 118–129. https://doi.org/10.1016/j.enggeo.2016.10.004.

Khan, M. S., M. Nobahar, M. Stroud, S. Ferguson, and J. Ivoke. 2022. "Performance evaluation of a highway slope on expansive soil in Mississippi." *Int. J. Geomech.* 22 (1): 05021005. https://doi.org/10.1061/(ASCE)GM.1943-5622.0002240.

Khan, S., J. Ivoke, and M. Nobahar. 2019. "Coupled effect of wet-dry cycles and rainfall on highway slope made of Yazoo clay." *Geosciences* 9 (8): 341. https://doi.org/10.3390/geosciences9080341.

Mai, C., K. Konakli, and B. Sudret. 2017. "Seismic fragility curves for structures using non-parametric representations." *Front. Struct. Civ. Eng.* 11 (Jun): 169–186. https://doi.org/10.1007/s11709-017-0385-y.

McKenna, G., S. A. Argyroudis, M. G. Winter, and S. A. Mitoulis. 2021. "Multiple hazard fragility analysis for granular highway embankments: Moisture ingress and scour." *Transp. Geotech.* 26 (Jan): 100431. https://doi.org/10.1016/j.trgeo.2020.100431.

Micheli, L., A. Alipour, S. Laflamme, and P. Sarkar. 2019. "Performance-based design with life-cycle cost assessment for damping systems integrated in wind excited tall buildings." *Eng. Struct.* 195 (Sep): 438–451. https://doi.org/10.1016/j.engstruct.2019.04.009.

Micheli, L., L. Cao, S. Laflamme, and A. Alipour. 2020. "Life-cycle cost evaluation strategy for high-performance control systems under uncertainties." *J. Eng. Mech.* 146 (2): 04019134. https://doi.org/10.1061/(ASCE)EM.1943-7889.0001711.

NOAA (National Oceanic and Atmospheric Administration). 2013. "Precipitation-frequency Atlas of the United States." Accessed May 28, 2023. https://hdsc.nws.noaa.gov/pfds.

Nobahar, M., M. S. Khan, and J. Ivoke. 2020. "Combined effect of rainfall and shear strength on the stability of highway embankments made of Yazoo clay in Mississippi." *Geotech. Geol. Eng.* 38 (Jun): 2787–2802. https://doi.org/10.1007/s10706-020-01187-8.

Nobahar, M., M. S. Khan, J. Ivoke, and F. Amini. 2019. "Impact of rainfall variation on slope made of expansive Yazoo clay soil in Mississippi." *Transp. Infrastruct. Geotechnol.* 6 (Dec): 318–336. https://doi.org/10.1007/s40515-019-00083-w.

Pan, Y., A. K. Agrawal, and M. Ghosn. 2007. "Seismic fragility of continuous steel highway bridges in New York State." *J. Bridge Eng.* 12 (6): 689–699. https://doi.org/10.1061/(ASCE)1084-0702(2007)12:6(689).

Porter, K., R. Hamburger, and R. Kennedy. 2007. "Practical development and application of fragility functions." In *Structural engineering research frontiers*, 1–16. Reston, VA: ASCE.

Porter, K., R. Kennedy, and R. Bachman. 2006. *Developing fragility functions for building components for ATC-58*. Rep. No. ATC-58. Redwood City, CA: Applied Technology Council.

Rohmer, J., P. Gehl, M. Marcilhac-Fradin, Y. Guigueno, N. Rahni, and J. Clément. 2020. "Non-stationary extreme value analysis applied to seismic fragility assessment for nuclear safety analysis." *Nat. Hazards Earth Syst. Sci.* 20 (5): 1267–1285. https://doi.org/10.1061/(ASCE)1084-0702(2007)12:6(689).

Rosowsky, D. V., and B. R. Ellingwood. 2002. "Performance-based engineering of wood frame housing: Fragility analysis methodology." *J. Struct. Eng.* 128 (1): 32–38. https://doi.org/10.1061/(ASCE)0733-9445(2002)128:1(32).

Shinozuka, M., M. Q. Feng, H.-K. Kim, and S.-H. Kim. 2000a. "Nonlinear static procedure for fragility curve development." *J. Eng. Mech.* 126 (12): 1287–1295. https://doi.org/10.1061/(ASCE)0733-9399(2000)126:12(1287).

Shinozuka, M., M. Q. Feng, J. Lee, and T. Naganuma. 2000b. "Statistical analysis of fragility curves." *J. Eng. Mech.* 126 (12): 1224–1231. https://doi.org/10.1061/(ASCE)0733-9399(2000)126:12(1224).

Shinozuka, M., S.-H. Kim, S. Kushiyama, and J.-H. Yi. 2002. "Fragility curves of concrete bridges retrofitted by column jacketing." *Earthquake Eng. Eng. Vibr.* 1 (2): 195–205. https://doi.org/10.1007/s11803-002-0065-2.

Singhal, A., and A. S. Kiremidjian. 1996. "Method for probabilistic evaluation of seismic structural damage." *J. Struct. Eng.* 122 (12): 1459–1467. https://doi.org/10.1061/(ASCE)0733-9445(1996)122:12(1459).

Taylor, A. 2005. "Mineralogy and engineering properties of the Yazoo clay formation." Master's thesis, Dept. of Geosciences, Mississippi State Univ.

Tohari, A., M. Nishigaki, and M. Komatsu. 2007. "Laboratory rainfall-induced slope failure with moisture content measurement." *J. Geotech. Geoenviron. Eng.* 133 (5): 575–587. https://doi.org/10.1061/(ASCE)1090-0241(2007)133:5(575).

USACE. 2021. *Slope stability.* Rep. No. EM 1110-2-1902. Washington, DC: USACE.

van de Lindt, J. W., and T. N. Dao. 2009. "Performance-based wind engineering for wood-frame buildings." *J. Struct. Eng.* 135 (2): 169–177. https://doi.org/10.1061/(ASCE)0733-9445(2009)135:2(169).

van Genuchten, M. T. 1980. "A closed-form equation for predicting the hydraulic conductivity of unsaturated soils." *Soil Sci. Soc. Am. J.* 44 (5): 892–898. https://doi.org/10.2136/sssaj1980.03615995004400050002x.

Vorogushyn, S., B. Merz, and H. Apel. 2009. "Development of dike fragility curves for piping and micro-instability breach mechanisms." *Nat. Hazards Earth Syst. Sci.* 9 (4): 1383–1401. https://doi.org/10.5194/nhess-9-1383-2009.

Wang, Z., L. Micheli, F. Ubertini, and S. Laflamme. 2022. "Risk-informed design optimization of vertically distributed tuned liquid wall dampers for multihazard mitigation." *J. Struct. Eng.* 148 (3): 04021295. https://doi.org/10.1061/(ASCE)ST.1943-541X.0003282.

Wu, X. Z. 2015. "Development of fragility functions for slope instability analysis: Fragility functions for slope instability analysis." *Landslides* 12 (1): 165–175. https://doi.org/10.1007/s10346-014-0536-3.

Zentner, I., M. Gündel, and N. Bonfils. 2017. "Fragility analysis methods: Review of existing approaches and application." *Nucl. Eng. Des.* 323 (Nov): 245–258. https://doi.org/10.1016/j.nucengdes.2016.12.021.